The Journal of Physical Chemistry Letters

Letter

Atomically Intercalating Tin Ions into the Interlayer of Molybdenum Oxide Nanobelt Toward Long-cycling Lithium Battery

Chuanqiang Wu, Hui Xie, Dongdong Li, Daobin Liu, Shiqing Ding, Shi Tao, Heng Chen, Qin Liu, Shuangming Chen, Wangsheng Chu, Bo Zhang, and Li Song

J. Phys. Chem. Lett., **Just Accepted Manuscript** • DOI: 10.1021/acs.jpclett.7b03374 • Publication Date (Web): 01 Feb 2018

Atomically Intercalating Tin Ions into the Interlayer of Molybdenum Oxide Nanobelt toward Long-Cycling Lithium Battery

Chuanqiang Wu,[†,+] Hui Xie,[†,+] Dongdong Li,[‡] Daobin Liu,[†] Shiqing Ding,[†] Shi Tao[§], Heng Chen,[‡] Qin Liu,[†] Shuangming Chen,[†] Wangsheng Chu,[†] Bo Zhang,[‡] and Li Song*[†]*

[†]National Synchrotron Radiation Laboratory, CAS Center for Excellence in Nanoscience, University of Science and Technology of China, Hefei, Anhui 230029, P. R. China

[‡]Institute of Amorphous Matter Science, School of Materials Science and Engineering, Hefei University of Technology, Hefei, Anhui 230009, P. R. China

[§]Department of Physics and Electronic Engineering, Jiangsu Lab of Advanced Functional Materials, Changshu Institute of Technology, Changshu, Jiangsu 215500, China

Corresponding Author

*Email: csmp@ustc.edu.cn (S.C.), song2012@ustc.edu.cn (L.S.)

ABSTRACT: Atomic intercalation of different agents into two-dimensional layered materials can engineer the intrinsic structure at the atomic scale and thus tune the physical and chemical properties for specific applications. Here we successfully introduce tin (Sn) atoms into the interlayer of α-MoO_3 nanobelts forming a new MoO_3-Sn intercalation with ultra-stable structure.

Combining with theoretical calculations, our synchrotron radiation-based characterizations and electron microscope observations clearly reveal that the intercalated Sn atoms could bond with five O atoms, forming a pentahedral structure. Subsequently, the Sn-O bonds induce a less distorted [MoO_6] octahedral structure, resulting in a unique structure that is distinct with pristine α-MoO_3 or any other Molybdenum oxides. Employing as anode for lithium-ion battery, the as-prepared MoO_3-Sn nanobelts display a much higher capacity of 520 $mAhg^{-1}$ at 500 mAg^{-1} than α-MoO_3 nanobelts (291 $mAhg^{-1}$), with a Coulombic efficiency of 99.5%. Moreover, owing to the strong intercalation from Sn ions, the MoO_3-Sn nanobelts pose superior cyclability, durability and reliability.

TOC GRAPHICS

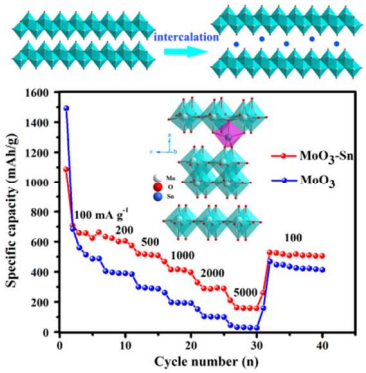

KEYWORDS: metal ions intercalation; MoO_3 nanobelt; micro-structure; EXAFS; lithium battery.

Two-dimentional (2D) layered materials have attracted considerable attention in the past decade for their excellent physical, chemical, electronic and optical properties with their various potential for technological applications as well as an abundant of unexplored fundamental science[1-11]. Typically, 2D layered materials exhibit strong in-plane covalent bonding and weak out-of-plane van der Waals interactions through the interlayer gap. Therefore different types of

intercalation agents can be intercalated into the interlayer space, without causing a chemical bond rupture and structure damage in 2D materials[12-18]. Such intercalations provide a facile way to create new types of multifunctional materials to promote the physical and chemical properties. For examples, the larger interlayer distance was reported to generate more active site and ion channels for chemical reactions[19,20]. The changed band structure induced by intercalatation can cause the promotion of conductivity and optical performance[21,22], which largely extends 2D layered material's applications for opto-electronic devices, energy storage and conversion, photoelectrocatalysis, etc.

As an energy storage device, Lithium-ion batteries (LIBs) have shown a high performance application for mobile electrical devices and electric vehicles due to high energy density and longer lifespan[23-29]. However, as the insertion/extraction of Li ions, the charge-discharge process often results in variations in the layer distances, which is accompanied by successive phase transitions. In addition, low stability of circulation at high rates prevents the LIBs to accomplish the industry needs of these new applications[30-32]. Therefore, looking for new materials or designing new structure to develop LIBs has become a urgent need. Fortunately, by controlling the morphology and structure of the developed 2D layered materials, the expanded interlayer spacing and reduced distance for Li^+ and electron diffusion can improve the performance of LIBs. A recent study revealed that the effect of different interlayer cations on the storage capacity and cycling stability of layered manganese oxide (MnO_2)[33], it's influenced by the interlayer spacing and the potential Coulomb repulsion forces between cations. These results provide promising ideas for the efficient design of advanced electrodes for LIBs.

Among various candidates, layered molybdenum trioxide (MoO_3) was carefully investigated as an anode for LIBs due to its good chemical stability and unique 2D layered structure. In fact,

MoO_3 nanobelts were considered to be a promising anode material for rechargeable LIBs because of the efficient electron transport pathways and facile strain relaxation[32,34,35]. However, the undesirable ionic and electronic conductivity of MoO_3 leads to poor electrochemical kinetics and a serious capacity fading during cycling, especially at high rates failing to achieve theoretical capacity by using pure sample. Orthorhombic MoO_3 (α-MoO_3) phase is a thermodynamically stable phase than monoclinic MoO_3 (β-MoO_3) and hexagonal MoO_3 (h-MoO_3) phases. The α-MoO_3 phase is constituted by corner-sharing [MoO_6] octahedra along [001] and [100] directions. Two sublayers are stacked together by sharing the edges of octahedra along the [001] direction to form a layer. Moreover, an anisotropic structure with layers along the [010] direction with van der Waals interaction leads to the formation of α-MoO_3 with a two-dimensional layer structure, thus it allows guest atoms (Li^+, M^{n+}) insert into the layers by intercalation[32,36,37]. Furethermore, the [MO_6] octahedron in α-MoO_3 is significantly distorted, there is a clear tendency towards molybdenyl MO_2^{2+} formation[38]. Traditionally, tin and tin oxide are good candidates for an anode of lithium-ion batteries, but they have relatively low theoretical capacity compared with α-MoO_3 (Sn: 992mAhg-1, SnO_2: 782mAhg-1, α-MoO_3: 1111mAhg-1) [23,35,39] Considering of this, we assume α-MoO_3 as a good host for tin metal ions within its inner planes to create Mo-O-Sn-O-Mo structure in order to protect the structural stability and enhance conductivity of LIBs. To demonstrate the predication, we synthesized white single crystalline α-MoO_3 nanobelts and Sn ions intercalated α-MoO_3 nanobelts (MoO_3-Sn nanobelts) by using a facile hydrothermal method. Our theoretical calculations and experimental results confirmed the atomical intercalation of tin atoms in the interlayer of molybdenum oxide, which demonstrate a promising anode candidate for LIBs with high capacitance and excellent long cycling performance.

Typically, the MoO_3-Sn nanobelt was synthesized by using a simple hydrothermal method in acetone solution. Figure 1a illustrates the synthesis process of our samples. Firstly, the synthesized α-MoO_3 nanobelt was dispersed into acetone solution and ultrasonic to achieve a uniform mixture. Then, the tartaric acid and stannous chloride dihydrate were dissolved into the mixture with heating and continuously stirring. During the reaction, the solution appeared obvious color change from white to blue. Finally, the blue product was obtained. This reaction has two processes: firstly, zerovalent Sn atoms were inserted into the interlayer of α-MoO_3 via a disproportionation redox reaction of Sn(II), according to the previous reports[40-42]; afterward, the Sn atoms in the interlayer interacted with the oxygen atoms of the layer to form a stable structure which will be discussed in the following section.

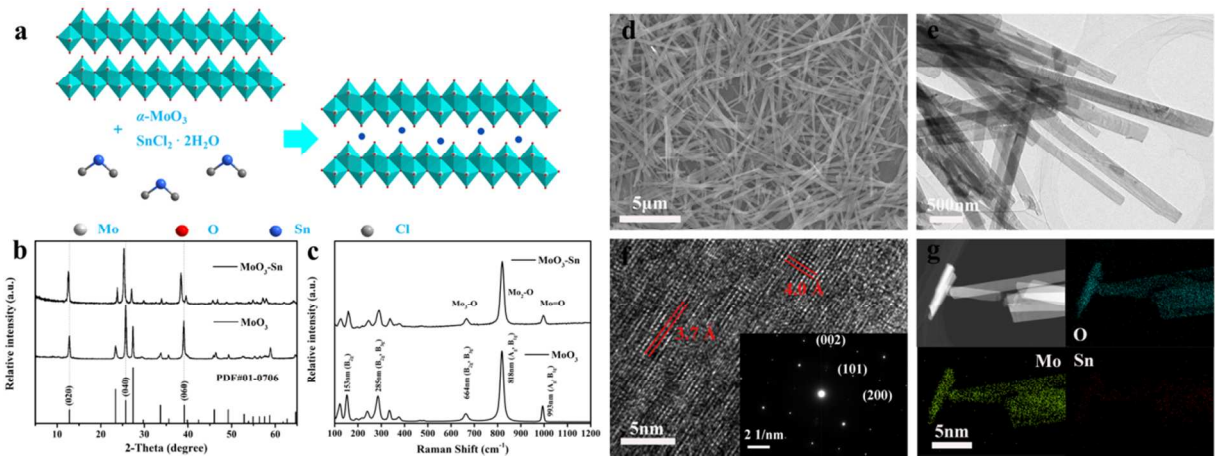

Figure 1. (a) Illustration of the synthesis process of the MoO_3-Sn nanobelts, (b) XRD patterns of α-MoO_3 nanobelts, MoO_3-Sn nanobelts and standard card PDF#01-0706, (c) Raman spectrum (532.2 nm excitation) of α-MoO_3 nanobelts and the MoO_3-Sn nanobelts, (d-g) SEM, TEM , HRTEM (selected area electron diffraction pattern inserted) and STEM-EDS element mapping images of MoO_3-Sn nanobelts.

First of all, X-ray diffraction results show the crystal structures and phases of the pure α-MoO_3 nanobelts and the MoO_3-Sn nanobelts. As shown in Figure 1b, all diffraction peaks can be exclusively indexed as the orthorhombic α-MoO_3 phase and a space group of Pbnm (PDF#01-0706), suggesting a high purity of the products. The strong intensity of the diffraction peaks at 12.82°, 25.73°, 39.13°, which can be indexed to (020), (040), (060) planes of α-MoO_3 nanobelts, indicates that there is a preferred orientation on the ac plane[24,30,36,343]. In the meanwhile, Raman spectroscopy of α-MoO_3 nanobelts and the MoO_3-Sn nanobelts was collected under 532.3 nm excitation, which shown in Figure 1c in the range 100-1200 cm^{-1} [39,34,44,45]. Compared with *α*-MoO_3 nanobelts, there is no obvious change from Raman spectrum after Sn atoms intercalation. This suggests that the MoO_3-Sn nanobelts maintained the original *α*-MoO_3 structure without obvious changes, which is consistent with the XRD characterization. The corresponding SEM images of *α*-MoO_3 nanobelts and MoO_3-Sn nanobelts are shown in Figure S1a (Supplementary information) and Figure 1d. It can be observed that before and after intercalation, the nanobelts keep the morphology with width of 200-500 nm and lengths of about 10 μm. To further understand the morphology and micro-structure of samples, transmission electron microscopy (TEM) and high-resolution transmission electron microscopy (HRTEM) were employed. As shown in Figure S1b and Figure 1e, both of *α*-MoO_3 nanobelts and MoO_3-Sn nanobelts have the similar appearance without any impurity, indicating the introduction of Sn atoms did not affect the morphology. The smooth surface was retained after the intercalation which is in good agreement with SEM observations. By magnified the HRTEM image (Figure 1f), MoO_3-Sn nanobelts display two set of obvious crystal lattice fringes, corresponding to the 0.37 Å and 4.0 Å atomic spacings, which are assigned to the {001} and {100} planes respectively, consistent with previous reports of *α*-MoO_3 nanobelts[29,32,42,46,47]. The SAED pattern of MoO_3-Sn nanobelts

can be attributed to the [010] zone axis, according to HRTEM analysis. It reveals the single-crystalline nature of the MoO_3-Sn nanobelts. The SAED of α-MoO_3 nanobelt in Figure S1c displays similar patterns. Based on the above electron microscope analys, we can suggest that the nanobelts grow along the [001] direction. The chemical composition of MoO_3-Sn nanobelts was further probed by element mapping and energy dispersive spectroscopy (EDS) analyses. Figure S1d indicates three elements of O, Mo, and Sn in the as-synthesized samples. According to EDS analysis, the content of Sn element in MoO_3 nanobelts is 1.68 at% (see Table S1). The elemental mapping images show the homogeneous distribution of three elements in the whole nanobelts (see Figure 1g). According to these analysis results, it can be concluded that the intercalated Sn atoms are uniform distribution in the interlayers of nanobelts, and the host α-MoO_3 maintains the original structure.

X-ray photoelectron spectroscopy (XPS) was conducted to analyze the elemental composition, content and chemical state of the α-MoO_3 nanobelts and MoO_3-Sn nanobelts. Figure 2a shows the high resolution XPS spectra of Mo 3d of α-MoO_3 nanobelts and MoO_3-Sn nanobelts. The XPS spectrum of Mo 3d in the α-MoO_3 nanobelts displays two characteristic peaks, located at 233.1 eV and 236.3 eV arising from Mo (VI) $3d_{5/2}$ and Mo (VI) $3d_{3/2}$ orbital, which is similar to the previous reports[28,48]. Meanwhile, MoO_3-Sn nanobelts show the similar shape with Mo 3d peaks located at 232.8 eV and 236.0 eV. However, there are obvious downshifts to the lower binding energy compared with α-MoO_3 nanobelts, implying Mo atoms gain some electrons. The XPS of Sn 3d in the MoO_3-Sn nanobelts was also tested (Figure 2b), which displays two peaks at about 486.7 eV and 495.3 eV attributed to the Sn (IV) $3d_{5/2}$ and Sn (IV) $3d_{3/2}$, respectively[39]. Base on the reaction process, it can be reasonably proposed that the intercalated zerovalent Sn atoms combined with the oxygen atoms of α-MoO_3 accompanied by electron transfer, and then

these Sn atoms lost some electrons to state of nearly four valence. Considering the detection of XPS technique, we also obtained the content of Sn in MoO_3 nanobelts is 1.48 at% (see Table S1), consistent with the EDS analysis.

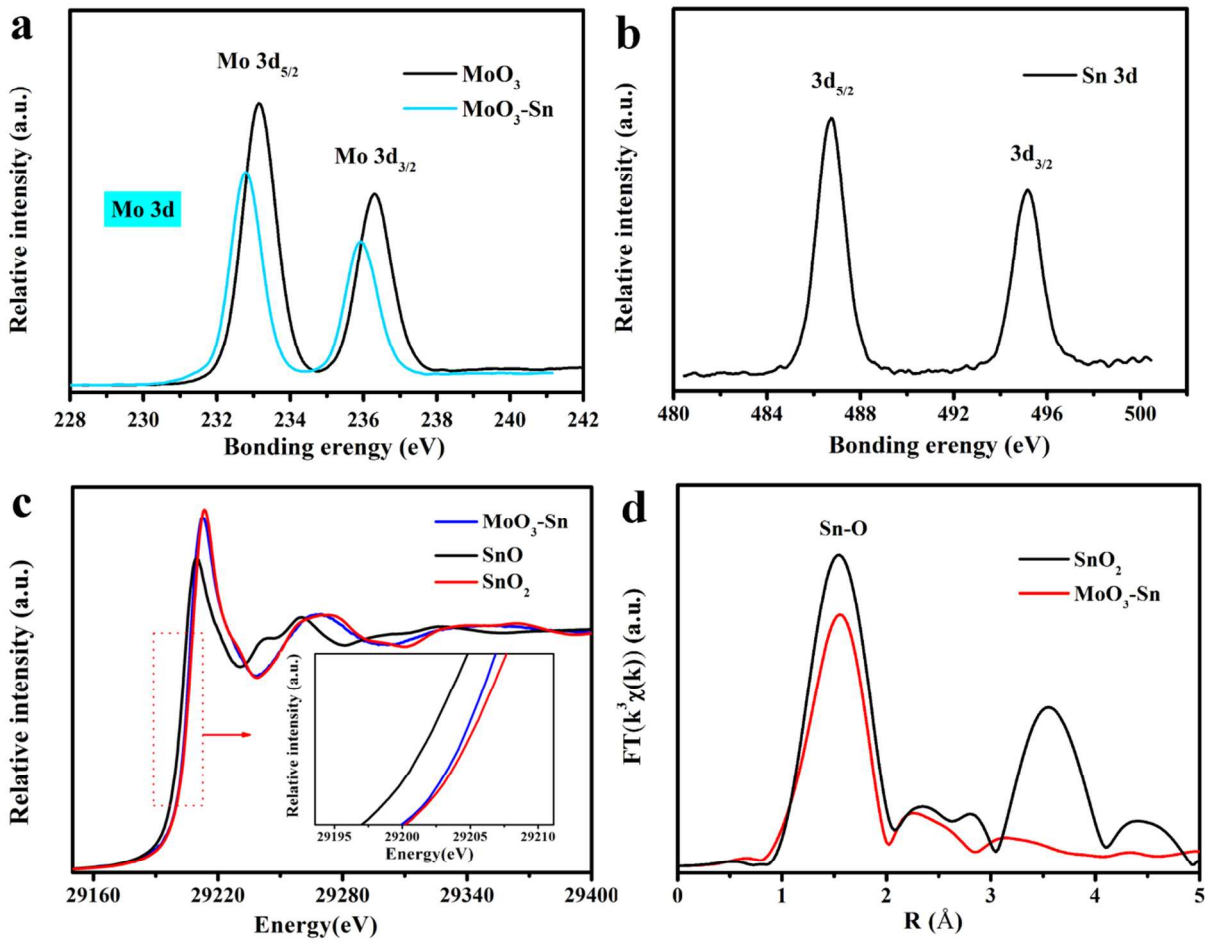

Figure 2. (a, b) XPS spectra of α-MoO_3 nanobelts and MoO_3-Sn nanobelts Mo 3d peak and Sn 3d peak. XANES spectra of Sn edge (c) and (d) the corresponding FT analyses reveal the Sn-O bond length and coordination state for SnO_2 and MoO_3-Sn nanobelts.

In order to further identify the microstructure of Sn atoms in the interlayer of α-MoO_3 nanobelts, we used the synchrotron radiation-based X-ray absorption fine structure spectroscopy (XAFS) which can investigate local bond lengths and coordination environment of a given

element. Figure S2a shows the XANES spectra of Mo edge and the corresponding Fourier-transformed (FT) EXAFS spectra revealing the Mo-O bond length and coordination state for MoO_3 foil, α-MoO_3 nanobelts and MoO_3-Sn nanobelts. It indicates that after introduction of Sn atoms, the microstructure of MoO_3 nanobelts has not been damaged. This conclusion is consistent with the previous analysis. However, in the real space, there is a difference of Mo-O bond at the second peak in the Figure S2b, indicating the coordination number of Mo-O has a little increase than Sn atoms intercalation before. It means the structural change of [MoO_6] octahedral due to the intercalation of Sn atoms. The length of Mo-O bond has a slight blue shift, indicating the average bond length is shorter. Figure 2c displays XANES spectra of Sn K-edge of SnO, SnO_2 and MoO_3-Sn nanobelts. It can be observed that the structure of Sn in the MoO_3-Sn nanobelts is close to SnO_2 rather than SnO. It is consistent with the analysis of XPS. The Sn atoms exist in nearly four valence state. The FT curves of SnO_2 and MoO_3-Sn nanobelts shown in Figure 2d indicate the SnO_2 and MoO_3-Sn nanobelts have the same Sn-O bond, but the coordination number of Sn-O in the MoO_3-Sn nanobelts is less than SnO_2. To obtain quantitative structural information of Sn atoms in the nanobelts, a least-squares curve parameter method was performed. The fitting results are summarized in Figure S3 and Table S2. According to the fitting data, it can be concluded that the intercalated Sn atoms in the interlayer of MoO_3 nanobelts are bonding with O atoms. The Sn-O bond length is about 2.05 Å and the coordination number is 5.2. The structure of [MoO_6] octahedral is affected by Sn atoms due to the interaction between Sn atoms and O atoms.

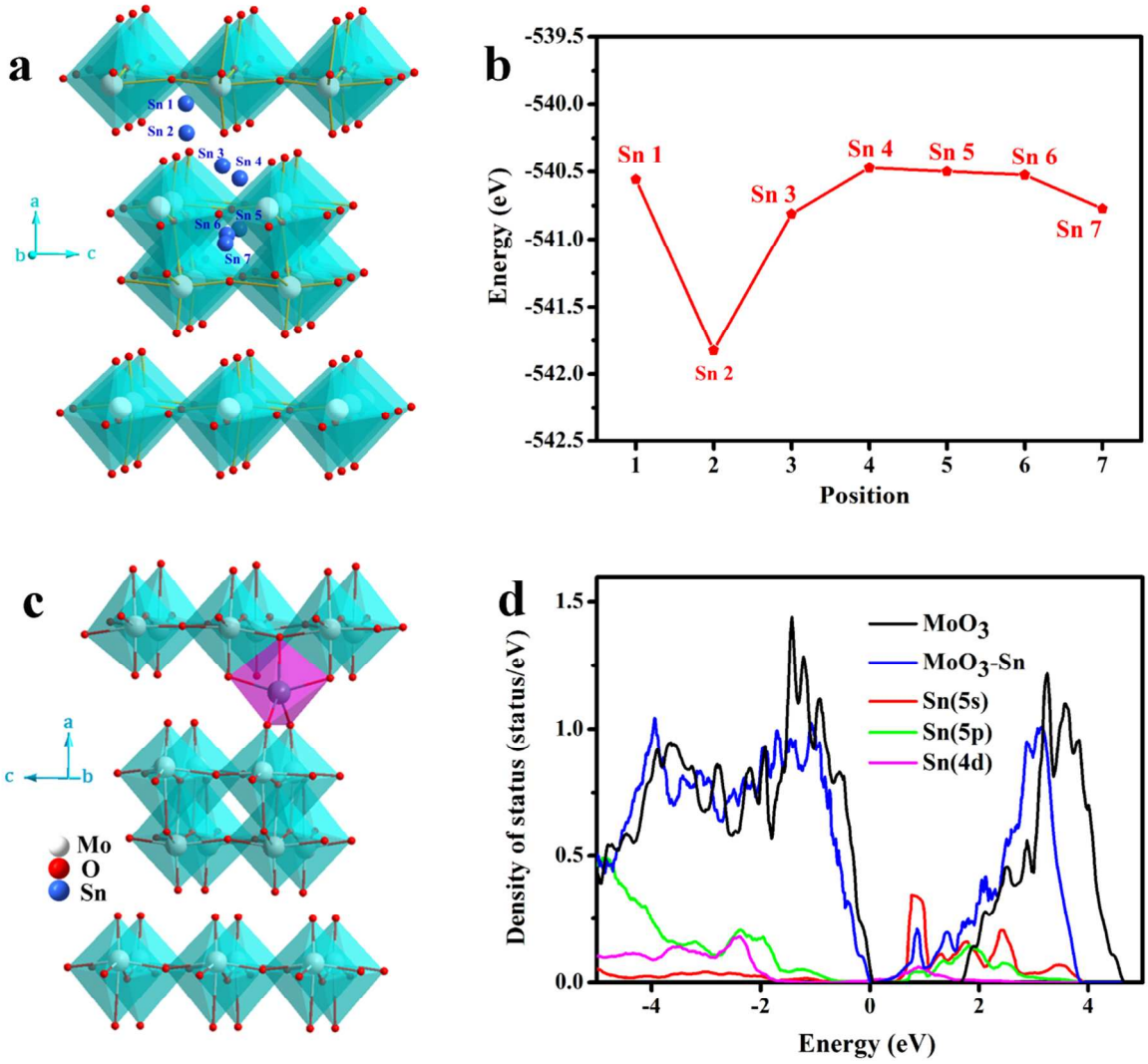

Figure 3. (a) Assumptions of different Sn atomic positions in MoO_3 structure, (b) related the total energy of different Sn atomic positions, (c) the optimum structure of (Sn 2), (d) the calculated total densities of states of α-MoO_3 and MoO_3-Sn structure.

Periodic DFT code VASP calculations were further carried out to understand the Sn atomic occupying information. We have assumed seven different Sn atomic positions as shown in Figure 3a. According to the structure of each Sn atoms occupies position, we calculated the total energy at different situations. Figure 3b displays the obtained calculation result, we can see that

the lowest total energy of -541.82 eV was obtained when Sn atoms locate at the position (Sn 2) (Different model of the Sn atoms bonding environment and total energy shown in Figure S4 and Table S3). It indicates that (Sn 2) is the most stable structure in the seven hypotheses. The optimum structure of (Sn 2) displayed in the Figure 3c shows that the intercalated Sn atoms in the interlayer of MoO_3 structure combines with 5 O atoms forming a pentahedral structure with the bonding length of 2.06 Å, consistent with the EXAFS analysis result. Besides, according to the calculation result, the Mo-O bond length of [MoO_6] octahedral was obtained (shown in Table S4). Compared with α-MoO_3 nanobelts, the Mo-O average bond length of MoO_3-Sn nanobelts becomes shorter and more average after the intercalation of Sn atoms, consistent with the EXAFS analysis result. Therefore, the [MoO_6] octahedral in MoO_3 will be less distorted and more stable after the Sn intercalation. The calculated total densities of states of α-MoO_3 and MoO_3-Sn structure are shown in Figure 3d. It can be clearly observed that the impurity states exist in the band gap, which is mainly contributed by Sn atoms. The impurity states services as a donor and enhances the density of charge carrier. By means of the detailed calculation, each Mo atom gains 0.032 electrons after the intercalation, resulting in the system conduction band minimum (CBM) position reduce and the forbidden band width decrease, as well as the electrical conductivity of sample increases (Figure S5).

As mentioned above, the poor electrochemical kinetics and serious capacity fading during cycling limite the application of α-MoO_3 in LIBs field. However, the intercalated Sn atoms enhance the structural stability and electroconductibility of α-MoO_3, which motivate us to investigate as-prepared MoO_3-Sn nanobelts for LIB application. As shown in Figure 4a, the rate performance of α-MoO_3 nanobelts and MoO_3-Sn nanobelts were studied at different cycling rates. Clearly, the MoO_3-Sn nanobelts exhibit much better performance with average initial discharge

capacity of 657, 602, 520, 411, 329, 159 mAh g^{-1} at current density of 100, 200, 500, 1000, 2000, 5000 mA g^{-1}, respectively, which is almost twice higher than the initial capacity of α-MoO_3 nanobelts at high rates. It is worth noting that the discharge capacity can still reach 518 mAh g^{-1} when the current density changes back to 100 mA g^{-1}. This result suggests a high rate capability and good stability of the LIBs with MoO_3-Sn nanobelts electrodes. Figure 2b displays the discharge/charge voltage profiles of the MoO_3-Sn nanobelts at a current density of 500 mA g^{-1} over a voltage range from 0.01 to 3.0 V. It can be observed that the charge and discharge capacity of MoO_3-Sn nanobelts electrode can reach 537 and 896 mAh g^{-1} in the first cycle, and the coulombic efficiency is estimated as 60.1%. In the following cycles, the coulombic efficiency rises up to 99%, and remains higher than 99%. Due to the activation process, the capacity decreases at the beginning, and then recovers as the cycle test. After 300 cycles, the discharge and charge capacity can still remain at 500.1 and 505.5 mAh g^{-1}. Even until 500 cycles, it still maintains a high capacity. The cycling performance of the α-MoO_3 nanobelts and MoO_3-Sn nanobelts at a current density of 500 mA g^{-1} in 200 cycles is shown in Figure 4c. It can be seen that compared with the α-MoO_3 nanobelts, MoO_3-Sn nanobelts display the higher cycling capacity, consistent with the rate performance test. Furthermore, in order to prove the stability of MoO_3-Sn nanobelts electrodes, we tested the electrodes for 200 cycles at 100 mA g^{-1} and 500 cycles at 500 and 1000 mA g^{-1} (Figure S6). It further demonstrates the cyclic stability of MoO_3-Sn nanobelts electrodes at high rates.

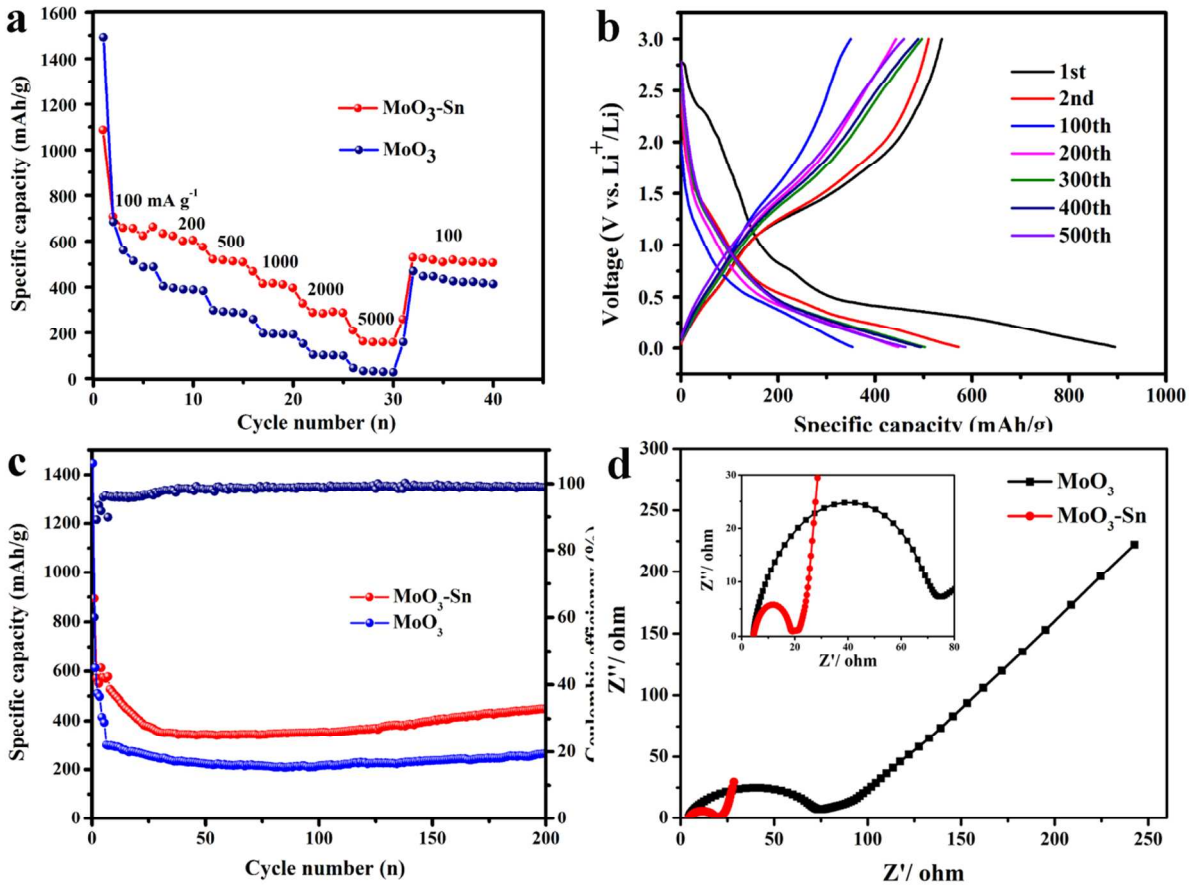

Figure 4. (a) The rate performance of α-MoO_3 nanobelts and MoO_3-Sn nanobelts at different cycling rates, (b) the discharge/charge voltage profiles of the MoO_3-Sn nanobelts at a current density of 500 mA g-1 over a voltage range from 0.01 to 3.0 V, (c) The cycling performance of the α-MoO_3 nanobelts and MoO_3-Sn nanobelts at a current density of 500 mA g-1, (d) electrochemical impedance spectroscopy (EIS) analysis of MoO_3 nanobelts and MoO_3-Sn nanobelts.

The significantly enhanced rate and cyclic performance of MoO_3-Sn nanobelts electrodes may be closely related to their excellent conductivity, which has been further confirmed by electrochemical impedance spectroscopy (EIS) analysis. Figure 4d shows Nyquist plots of the two samples over the frequency range from 100 kHz to 0.01 Hz. It clearly shows that both the

nyquist curves compose two parts, a semicircle in the high frequency region and a straight line in the low frequency region. The semicircle is related to the charge-transfer resistance (Rct) and the double-layer capacitance between the electrolyte and anode (Cdl). The inclined line is the Warburg impedance (Zw), which is associated with the Li^+ ion diffusion in the bulk electrode active particles[49]. Obviously, the diameter of the semicircle of the MoO_3-Sn nanobelts electrode is much smaller than that of α-MoO_3 nanobelts electrode, suggesting a lower charge-transfer resistance of the MoO_3-Sn nanobelts. Apart from this, the impedance slope of the MoO_3-Sn nanobelts electrode is much higher than that of α-MoO_3 nanobelts, indicating a higher mobility of Li^+ ions in MoO_3-Sn nanobelts electrode. To further demonstrate this, we calculated the diffusion coefficient of Li^+ ion according to the EIS data (shown in Figure S7). As a result, the Li^+ ions diffusion coefficient of MoO_3-Sn nanobelts (7.28×10^{-13} cm^2s^{-1}) is much higher than that of α-MoO_3 nanobelts (3.32×10^{-14} cm^2s^{-1}). It is probably due to the intercalation of Sn atoms extending the layer spacing of α-MoO_3 nanobelts, resulting in the fast transmission of Li^+ ions. In addition, the intercalated of Sn atoms reduced the CBM, making the fast electronic transmission. In order to exclude the Sn atoms providing the LIB capacity, we made the XRD analysis of MoO_3-Sn nanobelts electrode after discharge. Figure S8 shows XRD patterns of MoO_3-Sn nanobelts electrode after Li insertion, it can be well indexed to Li_2MoO_4 (PDF#12-0763) and Cu (PDF#01-1241). There is no diffraction peak attributed to Li-Sn compounds, indicating the intercalated Sn did not participate in the charge and discharge reaction of MoO_3-Sn nanobelts electrode. Moreover, to confirm the cyclic stability of MoO_3-Sn nanobelts electrode, the cyclic voltammograms was carried out. Figure S9 displays the CV curves of α-MoO_3 nanobelts and MoO_3-Sn nanobelts with 1st, 2nd, 5th cycles. It shows the same peaks without any new peak, meaning the same electrochemical process during lithiation/delithiation process. Due

to the structure of MoO_3 nanobelts has a little change after the intercalation of Sn atoms, the peak position has a little deviation. The presence of Sn atoms stabilizes the structure of the α-MoO_3 nanobelts and leads to the cyclic stability increased.

In summary, we have successfully introduced Sn atoms into the interlayer of α-MoO_3 nanobelts, with the Sn-MoO_3 nanobelts retaining the original morphology and good structural satability without any damage except for the increase of layer spacing. The intercalated Sn atoms were uniform distributed in the interlayer of *α*-MoO_3 nanobelts. By means of the XAFS analysis and first-principle calculation, Sn atoms were clearly proved to be bonded with five O atoms forming a pentahedral structure with the Sn-O length of about 2.05 Å. Furthermore, the intercalated Sn atoms lead to a less distorted [MoO_6] octahedral structure due to the interaction between Sn atoms and O atoms, resulting in the structure of MoO_3 nanobelts more stable. The as-prepared MoO_3-Sn nanobelts displayed a much higher charge and discharge capacity and superior cyclic stability than the orighnal MoO_3 nanobelts in lithium battery performance. This can be ascribed to the intercalation of Sn atoms extending the layer spacing of α-MoO_3 nanobelts, leading to the fast transmission of Li^+ ions and electronics. This study provides a novel route to design new anode materials for LIB and other related applications.

ASSOCIATED CONTENT

Supporting Information. Material's synthesis and characterization, Electrochemical analysis and theoretical calculations, SAED patterns of *α*-MoO_3 nanobelts and the EDS analysis graphics of MoO_3-Sn nanobelts, The content of Sn element in MoO_3 nanobelts test by EDS and XPS, XAFS fitting curves and parameters, Different DFT model and total energy result of the Sn atoms bonding environment, The cycling performance of the MoO_3-Sn nanobelts. Plots

comparison of Z_{Re} vs $\omega^{-0.5}$ for α-MoO_3 nanobelts and MoO_3-Sn nanobelts. XRD patterns of MoO_3-Sn nanobelts after Li insertion. The CV curves of α-MoO_3 nanobelts and MoO_3-Sn nanobelts. The following files are available free of charge (PDF).

AUTHOR INFORMATION

[+] These authors contributed equally.

Notes

The authors declare no competing financial interest.

ACKNOWLEDGMENT

This work is financially supported in partly by MOST (2017YFA0303500, 2014CB848900), NSFC (U1532112, 11574280, 11605201), Innovative Research Groups of NSFC (Grant No.11621063), Anhui Provincial Natural Science Foundation (1708085QB27), CAS Interdisciplinary Innovation Team and CAS Key Research Program of Frontier Sciences (QYZDB-SSW-SLH018). L.S. acknowledges the recruitment program of global experts, the CAS Hundred Talent Program and Key Laboratory of Advanced Energy Materials Chemistry (Ministry of Education), Nankai University (111 project，B12015), Key Laboratory of the Ministry of Education for Advanced Catalysis Materials and Zhejiang Key Laboratory for Reactive Chemistry on Solid Surfaces (Zhejiang Normal University). The computational center of USTC is acknowledged for computational support. We thank the Shanghai synchrotron Radiation Facility (14W1, SSRF), the Beijing Synchrotron Radiation Facility (1W1B and soft-X-ray endstation, BSRF), the Hefei Synchrotron Radiation Facility (Photoemission, MCD and Catalysis/Surface Science Endstations, NSRL), and the USTC Center for Micro and Nanoscale Research and Fabrication for helps in characterizations.

REFERENCES

(1) Tan, C. L.; Cao, X. H.; Wu, X. J.; He, Q. Y.; Yang, J.; Zhang, X.; Chen, J. Z.; Zhao, W.; Han, S. K.; Nam, G. H.; Sindoro, M.; Zhang, H. Recent advances in ultrathin two-dimensional nanomaterials. *Chem. Rev.* **2017**, *117*, 6225-6331.

(2) Mannix, A. J.; Kiraly, B.; Hersam, M. C.; Guisinger, N. P. Synthesis and chemistry of elemental 2D materials. *Nat. Rev. Chem.* **2017**, *1*, 14-17.

(3) Xue, Y. H.; Zhang, Q.; Wang, W. J.; Cao, H.; Yang, Q. H.; Fu, L. Opening two-dimensional materials for energy conversion and storage: a concept. *Adv. Energy Mater.* **2017**, *7*, 1602684-1602706.

(4) Coleman, J. N.; Lotya, M.; O'Neill, A.; Bergin, S. D.; King, P. J.; Khan, U.; Young, K.; Gaucher, A.; De, S.; Smith, R. J.; Shvets, I. V.; Arora, S. K.; Stanton, G.; Kim, H. Y.; Lee, K.; Kim, G. T.; Duesberg, G. S.; Hallam, T.; Boland, J. J.; Wang, J. J.; Donegan, J. F.; Grunlan, J. C.; Moriarty, G.; Shmeliov, A.; Nicholls, R. J.; Perkins, J. M.; Grieveson, E. M.; Theuwissen, K.; McComb, D. W.; Nellist, P. D.; Nicolosi, V. Two-dimensional nanosheets produced by liquid exfoliation of layered materials. *Science*. 2011, *331*, 568-571.

(5) Lukatskaya, M. R.; Mashtalir, O.; Ren, Ch. E.; Dall'Agnese, Y.; Rozier, P.; Taberna, P. L.; Naguib, M.; Simon, P.; Barsoum, M. W.; Gogotsi, Y. Cation intercalation and high volumetric capacitance of two-dimensional titanium carbide. *Science*. **2013**, *341*, 1502-1505.

(6) Zhang, H. Ultrathin two-dimensional nanomaterials. *ACS Nano*. **2015**, *9*, 9451-9469.

(7) Chao, L.; Zhang, H. Two-dimensional transition metal dichalcogenide nanosheet-based composites. *Chem Soc Rev*. **2015**, *44*, 2713-2731.

(8) Bonaccorso, F.; Colombo, L.; Yu, G. H.; Stoller, M.; Tozzini, V.; Ferrari, A. C.; Ruoff, R. S.; Pellegrini, V. Graphene, related two-dimensional crystals, and hybrid systems for energy conversion and storage. *Science.* **2015**, *347*, 1246501-1246510.

(9) Xu, M. S.; Liang, T.; Shi, M. M.; Chen, H. Z. Graphene-like two-dimensional materials. *Chem. Rev*. **2013**, *113*, 3766-3798.

(10) Feng, J.; Sun, X.; Wu, C. Z.; Peng, L. L.; Lin, C. W.; Hu, S. L.; Yang, J. L.; Xie, Y. Metallic few-layered VS_2 ultrathin nanosheets: high two-dimensional conductivity for in-plane supercapacitors. *J. Am. Chem. Soc.* **2011**, *133*, 17832-17838.

(11) Naguib, M.; Halim, J.; Lu, J.; Cook, K. M.; Hultman, L.; Gogotsi, Y.; Barsoum, M. W. New two-simensional niobium and vanadium carbides as promising materials for Li-ion batteries. *J. Am. Chem. Soc.* **2013**, *135*, 15966-15969.

(12) Naguib, M.; Kurtoglu, M.; Presser, V.; Lu, J.; Niu, J. J.; Heon, M.; Hultman, L.; Gogotsi, Y.; Barsoum, M. W. Two-dimensional nanocrystals produced by exfoliation of Ti_3AlC_2. *Adv. Mater*. **2011**, *23*, 4248-4253.

(13) Takada, K.; Sakurai, H.; Takayama-M, E.; Izumi, F.; Dilanian, R. A.; Sasaki, T. Superconductivity in two-dimensional CoO2 layers. *Nature.* **2003**, *422*, 53-55.

(14) Zeng, Z. Y.; Yin, Z. Y.; Huang, X.; Li, H.; He, Q. Y.; Lu, G.; Boey, F.; Zhang, H. Single-layer semiconducting nanosheets: high-yield preparation and device fabrication. *Angew. Chem. Int. Ed.* **2011**, *50*, 11093-11097.

(15) Zeng, Z. Y.; Sun,T.; Zhu, J. X.; Huang, X.; Yin, Z. Y.; Lu, G.; Fan, Z. X.; Yan, Q. Y.; Hng, H. H.; Zhang, H. An effective method for the fabrication of few-layer-thick inorganic nanosheets. *Angew. Chem. Int. Ed.* **2012**, *51*, 9052-9056.

(16) Manish, C.; Shin, H. S.; Eda, G.; Li, L. J.; Loh, K. P.; Zhang, H. The chemistry of two-dimensional layered transition metal dichalcogenide nanosheets. *Nat. Chem.* **2013**, *5*, 263-275.

(17) Wang, Q. H.; Kalantar-Z, K.; Kis, A.; Coleman, J. N.; Strano, M. S. Electronics and optoelectronics of two-dimensional transition metal dichalcogenides. *Nat. Nanotech.* **2012**, *7*, 699-712.

(18) Xia, F. N.; Wang, H.; Xiao, D.; Dubey, M.; Ramasubramaniam, A. Two-dimensional material nanophotonics. *Nature Photon.* **2014**, *8*, 899-907.

(19) Chen, Z. X.; Leng, K.; Zhao, X. X.; Malkhandi, S.; Tang, W.; Tian, B. B.; Dong, L.; Zheng, L. R.; Lin, M.; Yeo, B. S.; Loh, K. P. Interface confined hydrogen evolution reaction in zero valent metal nanoparticles-intercalated molybdenum disulfide. *Nat. Commun*. **2017**, *8*, 14548-14556.

(20) Liu, Q.; Li, X. L.; Xiao, Z. R.; Zhou, Y.; Chen, H. P.; Khalil, A.; Xiang, T.; Xu, J. Q.; Chu, W. S.; Wu, X. J.; Yang, J. L.; Wang, Ch. M.; Xiong, Y. J.; Jin, Ch. H.; Ajayan, P. M.; Song, L. Stable metallic 1T-WS_2 nanoribbons intercalated with ammonia ions: the correlation between structure and electrical/optical properties. *Adv. Mater.* **2015**, *27*, 4837-4844.

(21) Liu, Q.; Li, X. L.; He, Q.; Khalil, A.; Liu, D. B.; Xiang, T.; Wu, X. J.; Song, L. Gram-scale aqueous synthesis of stable few-layered 1T-MoS_2 : applications for visible-light-driven photocatalytic hydrogen evolution. *Small.* **2015**, *41*, 5556-5564.

(22) Yao, J.; Koski, K. J.; Luo, W. D.; Cha, J. J.; Hu, L. B.; Kong, D. S.; Narasimhan, V. K.; Huo, K.; Cui, Y. Optical transmission enhacement through chemically tuned two-dimensional bismuth chalcogenide nanoplates. *Nat. Commun.* **2014**, *5*, 5670-5676.

(23) Zhang, G. H.; Zhu, J.; Zeng, W.; Hou, S. C.; Gong, F. L.; Li, F.; Li, C. C.; Duan, H. G. Tin quantum dots embedded in nitrogen-doped carbon nanofibers as excellent anode for lithium-ion batteries, *Nano Energy.* **2014**, *9*, 61-70.

(24) Hassan, M. F.; Guo, Z. P.; Chen, Z.; Liu, H. K. Carbon-coated MoO_3 nanobelts as anode materials for lithium-ion batteries. *J. Power. Sources.* **2010**, *195*, 2372-2376.

(25) Wang, W.; Qin, J. W.; Yin, Z. G.; Cao, M. H. Achieving fully reversible conversion in MoO_3 for lithium ion batteries by rational introduction of $CoMoO_4$. *ACS Nano.* **2016**, *10*, 10106-10116.

(26) Lee, S. H.; Kim, Y. H.; Deshpande, R.; Parilla, P. A.; Whitney, E.; Gillaspie, D. T.; Jones, K. M.; Mahan, A. H.; Zhang, Sh. B.; Dillon, A. C. Reversible lithium-ion insertion in molybdenum oxide nanoparticles. *Adv. Mater.* **2008**, *20*, 3627-3632.

(27) Yun, Q.; Lu, Q.; Zhang, X.; Tan, C.; Zhang, H. Three-dimensional architectures constructed from transition-metal dichalcogenide nanomaterials for electrochemical energy storage and conversion. *Angew. Chem. Int. Ed.* **2018**, *57*, 626-646.

(28) Cao, X. H.; Tan, C. L.; Sindoro, M.; Zhang, H. Hybrid micro-/nano-structures derived from metal-organic frameworks: preparation and applications in energy storage and conversion. *Chem. Soc. Rev.* **2017**, *46*, 2660-2677.

(29) Tao, T.; Glushenkov, A. M.; Zhang, C. F.; Zhang, H. Z.; Zhou, D.; Guo, Z. P.; Liu, H. K.; Chen, Q. Y.;. Hu, H. P; Chen, Y. MoO_3 nanoparticles dispersed uniformly in carbonmatrix: a high capacity composite anode for Li-ion batteries. J. *Mater. Chem.* **2011**, *21*, 9350-9355.

(30) Ma, F.; Yuan, A. B.; Xu, J. Q.; Hu, P. F. Porous α-MoO_3/MWCNT nanocomposite synthesized via a surfactant-assisted solvothermal route as a lithium-ion-battery high-capacity anode material with excellent rate capability and cyclability. *Appl. Mater. Interfaces.* **2015**, *7*, 15531-15541.

(31) Sen, U. K.; Mitra, S. Electrochemical activity of α-MoO_3 nano-belts as lithium-ion battery cathode**.** *RSC Advances.* **2012**, *2*, 11123-11131.

(32) Zhou, L.; Yang, L. C.; Yuan, P.; Zou, J.; Wu, Y. P.; Yu, C. Z. α-MoO3 nanobelts: A high performance cathode material for lithium ion batteries. *J. Phys. Chem. C* **2010**, *114*, 21868-21872.

(33) Lu, K.; Hu, Z. Y.; Xiang, Z. H.; Ma, J. Z.; Song, B.; Zhang, J. T.; Ma, H. Y. Cation intercalation in manganese oxide nanosheets: effects on lithium and sodium storage. *Angew. Chem. Int. Ed.* **2016**, *55*, 10448-10452.

(34) Lupan, O.; Trofim, V.; Cretu, V.; Stamov, I.; Syrbu, N. N.; Tiginyanu, I.; Mishra, Y. K.; Adelung, R. Investigation of optical properties and electronic transitions in bulk and

nano-microribbons of molybdenum trioxide. *J. Phys. D: Appl. Phys.* **2014**, *47*, 085302-085310.

(35) Xue, X. Y.; Chen, Z. H.; Xing, L. L.; Yuan, S.; Chen, Y. J. SnO2/α-MoO_3 core-shell nanobelts and their extraordinarily high reversible capacity as lithium-ion battery anodes. *Chem. Commun.* **2011**, *47*, 5205-5207.

(36) Han, B.; Lee, K. H.; Lee, W. Y.; Kim, S. J.; Park, H. C.; Hwang, B. M.; Kwak, D. H.; Park, K. W. MoO_3 nanostructured electrodes prepared via hydrothermal process for lithium ion batteries. *Int. J. Electrochem. Sci.* **2015**, *10*, 4232-4240.

(37) Scanlon, D. O.; Watson, G. W.; Payne, D. J.; Atkinson, G. R.; Egdell, R. G.; Law, D. S. L. Theoretical and Experimental Study of the Electronic Structures of $MoO_3$and MoO_2. *J. Phys. Chem. C* **2010**, *114*, 4636-4645.

(38) Chernova, N. A.; Roppolo, M.; Dillon, A. C.; Whittingham, M. S. Layered vanadium and molybdenum oxides: batteries and electrochromics. *J. Mater. Chem.* **2009**, *19*, 2526-2552.

(39) Ma, C. R.; Zhang, W. M.; He, Y. S.; Gong, Q.; Che, H. Y.; Ma, Z. F. Carbon coated SnO2 nanoparticles anchored on CNT as a superior anode material for lithium-ion batteries. *Nanoscale* **2016**, *8*, 4121-4126.

(40) Wang, M. j.; Koski, K. J. Reversible chemochromic MoO_3 nanoribbons through zerovalent metal intercalation. *ACS Nano.* **2015**, *9*, 3226-3233.

(41) Koski, K. J.; Wessells, C. D.; Reed, B. W.; Cha, J. J.; Kong, D. S. Cui, Y. Chemical intercalation of zerovalent metals into 2D layered Bi_2Se_3 Nanoribbons. *J. Am. Chem. Soc.* **2012**, *134*, 13773-13779.

(42) Koski, K. J.; Cha, J. J.; Reed, B. W.; Wessells, C. D.; Kong, D. S.; Cui, Y. High-density chemical intercalation of zero-valent copper into Bi_2Se_3 nanoribbons. *J. Am. Chem. Soc.* **2012**, *134*, 7584-7587.

(43) Xiao, X.; Peng, Z. H.; Chen, C.; Zhang, C. F.; Beidaghi, M.; Yang, Z. H.; Wu, N.; Huang, Y. H.; Miao, L.; Gogotsi, Y.; Zhou, J. Freestanding MoO_3-x nanobelt/carbon nanotube films for Li-ion intercalation pseudocapacitors. *Nano Energy*. **2014**, *9*, 355-363.

(44) Chen, X. H.; Lei, W. W.; Liu, D.; Hao, J.; Cui, Q. L.; Zou, G. T. Synthesis and characterization of hexagonal and truncated hexagonal shaped MoO_3 nanoplates. *J. Phys. Chem. C* **2009**, *113*, 21582-21585.

(45) Lupan, O.; Trofim, V.; Stamov, I.; Tiginyanu, I.; Mishra, Y. K.; Adelung, R. Investigation of optical properties and electronic transitions in bulk and nano-microribbons of molybdenum trioxide. *J. Phys. D: Appl. Phys.* **2014**, *47*, 085302-085309.

(46) Wang, K. K.; Wang, F. X.; Liu, Y. D.; Pan, G. B. Vapor growth and photoconductive property of single-crystalline MoO_3 nanosheets. *Materials Letters* **2013**, *102-103*, 8-11.

(47) Zheng, L.; Xu, Y.; Jin, D.; Xie, Y. Novel metastable hexagonal MoO_3 nanobelts: synthesis, photochromic, and electrochromic properties. *Chem. Mater.* **2009**, *21*, 5681-5690.

(48) Wang, C.; Wu, L. X.; Wang, H.; Zuo, W. H.; Li, Y. Y.; Liu, J. P. Fabrication and shell optimization of synergistic TiO_2-MoO_3 core-shell nanowire array anode for high energy and power density lithium-Ion batteries. *Adv. Funct. Mater.* **2015**, *25*, 3524-3533.

(49) Wu, Z. S.; Zhou, G. M.; Yin, L. C.; Ren, W. C.; Lia, F.; Cheng, H. M. Graphene/metal oxide composite electrode materials for energy storage. *Nano Energy*. **2012**, *1*, 107-131.